Quicker and More Zn^{2+} Storage Predominantly from the Interface

Yuhang Dai, Xiaobin Liao, Ruohan Yu, Jinghao Li, Jiantao Li, Shuangshuang Tan, Pan He, Qinyou An, Qiulong Wei, Lineng Chen, Xufeng Hong, Kangning Zhao, Yang Ren, Jinsong Wu, Yan Zhao, and Liqiang Mai*

Aqueous zinc-ion batteries are highly desirable for large-scale energy storage because of their low cost and high-level safety. However, achieving high energy and high power densities simultaneously is challenging. Herein, a VO_x sub-nanometer cluster/reduced graphene oxide (rGO) cathode material composed of interfacial V—O—C bonds is artificially constructed. Therein, a new mechanism is revealed, where Zn^{2+} ions are predominantly stored at the interface between VO_x and rGO, which causes anomalous valence changes compared to conventional mechanisms and exploits the storage ability of non-energy-storing active yet highly conductive rGO. Further, this interface-dominated storage triggers decoupled transport of electrons/Zn^{2+} ions, and the reversible destruction/reconstruction allows the interface to store more ions than the bulk. Finally, an ultrahigh rate capability (174.4 mAh g^{-1} at 100 A g^{-1}, i.e., capacity retention of 39.4% for a 1000-fold increase in current density) and a high capacity (443 mAh g^{-1} at 100 mA g^{-1}, exceeding the theoretical capacities of each interfacial component) are achieved. Such interface-dominated storage is an exciting way to build high-energy- and high-power-density devices.

1. Introduction

Electrochemical energy storage (EES) devices are great supports for electric vehicles, smart grids, and micro/nanodevices.[1,2] Lithium-ion batteries (LIBs) are the most used EES devices due to their high energy density but are significantly hindered by cost and safety issues.[3] Recently, aqueous zinc-ion batteries (AZIBs) have been considered as an alternative for LIBs due to their attractive properties, including a relatively low redox potential (−0.76 V vs standard hydrogen electrode), high specific capacity (819 mAh g^{-1}), and low cost due to the use of Zn metal anodes; moreover, the use of aqueous electrolytes brings high levels of safety, environmental friendliness, and high ionic conductivity.[4–6] Researchers have made numerous research efforts to design the cathode of AZIBs, for instance, by preintercalation strategies,[7,8] the development of anion redox activity,[9] and the construction of advantageous channels.[10] However, these strategies cannot break through the difficulty of achieving high energy density and high power density simultaneously, which is referred to as the Ragone conflict.[11]

The Ragone conflict is a representative concern in electrochemical energy storage devices. Typically, batteries deliver high theoretical capacity as the whole bulk is used to store ions (defined as the redox reaction in bulk). Unfortunately, the rate is diffusion-controlled and sluggish in bulk, which renders a low power density. In contrast, supercapacitors store charge by adsorbing electrolyte ions on the surface of the electrode material without ion diffusion (no redox reactions); hence, ion storage is rapid but rare.[12] Due to the discovery that interfacial nanocavities created by heterobonds or van der Waals interactions provide extra ion storage sites and faster ion migration channels,[13,14] while the European Large Scale Research Initiative "Battery 2030+" has pointed out that the interface in the battery is key to the effective use of the battery electrode material (see http://www.battery2030.eu), research interest has been focused on interface engineering to simultaneously increase the energy density and power density. To the best of our knowledge, all of these interfacial mass storage behaviors are based on the "job sharing" mechanism proposed by Maier.[15] Specifically, ions are stored in one phase while electrons are stored

Y. Dai, R. Yu, J. Li, Dr. J. Li, S. Tan, P. He, Prof. Q. An, L. Chen, X. Hong, Dr. K. Zhao, Prof. L. Mai
State Key Laboratory of Advanced Technology for Materials Synthesis and Processing
International School of Materials Science and Engineering
Wuhan University of Technology
Wuhan 430070, China
E-mail: mlq518@whut.edu.cn

X. Liao, Y. Zhao
State Key Laboratory of Silicate Materials for Architectures
Wuhan University of Technology
Wuhan 430070, China

R. Yu, Prof. J. Wu
Nanostructure Research Centre
Wuhan University of Technology
Wuhan 430070, China

Dr. Q. Wei
Fujian Key Laboratory of Materials Genome
College of Materials
Xiamen University
Xiamen 361005, China

Dr. Y. Ren
X-ray Science Division
Argonne National Laboratory
Lemont, IL 60439, USA

in another at the interface region to broaden mass storage forms. The derived studies include the interfacial storage of Li^{+} in Ru/Li$_2$O[16] and Ag^{+} in RbAg$_4$I$_5$/graphite.[17] Through decoupling electrons and ions, the use space of the material could be extended, which is promising for mitigating the trade-off between power density and energy density.

However, the previous interfacial "job sharing" mechanism was basically based on the possibility of thermodynamics[18,19] and lacked matching chemistry to construct composite materials with interfaces with sizes comparable to those of their bulk, such as atomic composite interfaces. Consequently, the previous interfacial storage methods contribute "extra" capacity rather than "large" capacity to the overall capacity,[14,20] which only marginally improves the electrochemical properties. An interface-dominated charge-storage contribution with high capacity and high rate remains unexplored. For the same reason, the interface jumbles with the bulk, which results in the lack of direct and in situ observations/characterizations of the interface-structural evolution and hinders further understanding of interfacial storage mechanisms. Moreover, the capacity as well as rate capability would be boosted if interfacial Zn^{2+} storage was involved in AZIBs.

Here, we provide a different strategy to realize Zn^{2+} storage predominantly originating from the interface and reveal a new energy storage form endowing nonfaradaic active reduced graphene oxide (rGO) with the ability to participate in faradaic electron transfer. Artificially constructed VO$_x$ sub-nanometer cluster/rGO composed of interfacial V−O−C bonds was selected as an example. For the first time, we found that interface-dominated Zn^{2+} storage triggers decoupled transport of electrons and Zn^{2+} ions in the interfacial region, which further gives rise to ion diffusion coefficients that are two orders of magnitude higher than those in the bulk. Moreover, we discovered an "interface breathing" effect, in which the reversible destruction/reconstruction of the interface enables the interface to store more Zn^{2+} than the bulk. Meanwhile, a unique interface pseudocapacitance mechanism is uncovered based on interface-dominated storage. Last, we achieve a remarkable electrochemical performance of quicker and more Zn^{2+} storage than conventional mechanisms, including an ultrahigh rate capability (174.4 mAh g^{−1} at 100 A g^{−1}, i.e., capacity retention of 39.4% for a 1000-fold increase in current density) and a high capacity (443 mAh g^{−1} at 100 mA g^{−1}, which exceeds the theoretical capacity of VO$_2$ and rGO). Interfacial storage is revealed to be controllable and universal. Based on such a new interface-dominated storage mechanism, we propose a promising way of constructing high-energy and high-power-density energy devices.

2. Results and Discussions

Atomic VO$_x$ clusters loaded on rGO (denoted as a VO$_x$ – G heterostructure) were synthesized to obtain a structure possessing heterogeneous interfaces with a thickness comparable to each component's thickness (detailed hydrothermal synthesis using conformal V$_2$O$_5$ sol sheet and rGO sheet precursors is shown in Figures S1 and S2, Supporting Information). We studied the morphology of the VO$_x$ – G heterostructure through high-angle annular dark-field (HAADF) scanning transmission electron microscopy (HAADF-STEM) (Figure S3, Supporting Information) and electron energy loss spectroscopy (EELS) (Figure S4, Supporting Information). According to these characterizations, the schematic diagram is presented in **Figure 1**a. VO$_x$ exhibits mainly sub-nanometer clusters (less than 1 nm in each dimension) and partial nanoclusters (a little larger than 1 nm). We then performed X-ray diffraction (XRD) analysis and showed that the nanocrystalline phase of the VO$_x$ nanoclusters is VO$_2$(B) (JCPDS NO:01-081-2392) (Figure S5, Supporting Information). However, the EELS spectra in Figure 1b reveal that V is in the form of V[4+] in the VO$_x$ nanocluster region ($\Delta E(O_K–L_3)$ = 10.2) and V[3+] in the VO$_x$ sub-nanometer cluster region ($\Delta E(O_K–L_3)$ = 10.8) (ref. [21]). To identify the origin of V[3+], we designed a sample of a mere VO$_2$ – rGO mixture that was physically mixed (denoted as VO$_2$ + G) for comparison. X-ray photoelectron spectroscopy (XPS) spectra of the C 1s core level show that the content of C−O bond[22] in the VO$_x$ – G heterostructure is apparently higher than that in VO$_2$ + G and VO$_2$ (Figure 1d), which is consistent with the XPS spectra of the O 1s core level and Fourier transform infrared (FTIR) spectra (Figure S7a,b, Supporting Information). The results indicate that there are many newly formed C−O bonds in the VO$_x$ – G heterostructure. Further analysis is incorporated with Raman analysis. The Raman spectra in Figure 1e show that peaks attributed to V3−O and V2−O stretching vibrations[23] shift to higher wavenumbers for the VO$_x$ – G heterostructure compared to VO$_2$ + G and VO$_2$, indicating that the abovementioned newly formed C−O bonds altered the electronic state of bridging oxygen in VO$_x$ clusters. In addition, different G-band positions in VO$_x$ – G heterostructure from VO$_2$ + G and VO$_2$ were observed (Figure S7c, Supporting Information), manifesting that the electron–phonon coupling of graphene is altered in the VO$_x$ – G heterostructure.[24] Last, the heterostructure of VO$_x$ – G is confirmed by showing different g-values of the VO$_x$ – G heterostructure than of VO$_2$ + G and VO$_2$ in the electron paramagnetic resonance spectra (Figure S7d, Supporting Information). Based on these characterizations, the specific form of the heterogeneous bond could be V−O−C bond. In addition, through density functional theory (DFT) calculations, we reveal that the Mulliken charge of interfacial V increases due to the formation of interfacial V−O−C bonds, while the upper V atoms show no charge difference (Figure S8, Supporting Information), thus explaining the origin of V[3+] in VO$_x$ sub-nanometer clusters and uncovering the heterostructure of VO$_x$ – G.

We focus on the VO$_x$ sub-nanometer cluster region, which has an interface size comparable to that of the VO$_x$ bulk. After zinc uptake in the VO$_x$ – G heterostructure (Figure S9, Supporting Information), the HAADF-STEM image at discharged state (Figure 1f) shows the Zn^{2+} ions are distributed adjacently to the isolated and irregularly distributed V atoms. To investigate the nature of the reaction, we carried out ex situ EELS and XPS investigations. As shown in Figure 1g, pristine V[3+] was oxidized to V[4+] after full discharge ($\Delta E_1(O_K–L_3)$ = 10.2) and reduced to V[3+] after full charge ($\Delta E_2(O_K–L_3)$ = 10.8), which was also confirmed by EELS valence mapping in the discharged state (Figure S10, Supporting Information) and the ex situ XPS spectra of the V 2p core level (Figure S11, Supporting
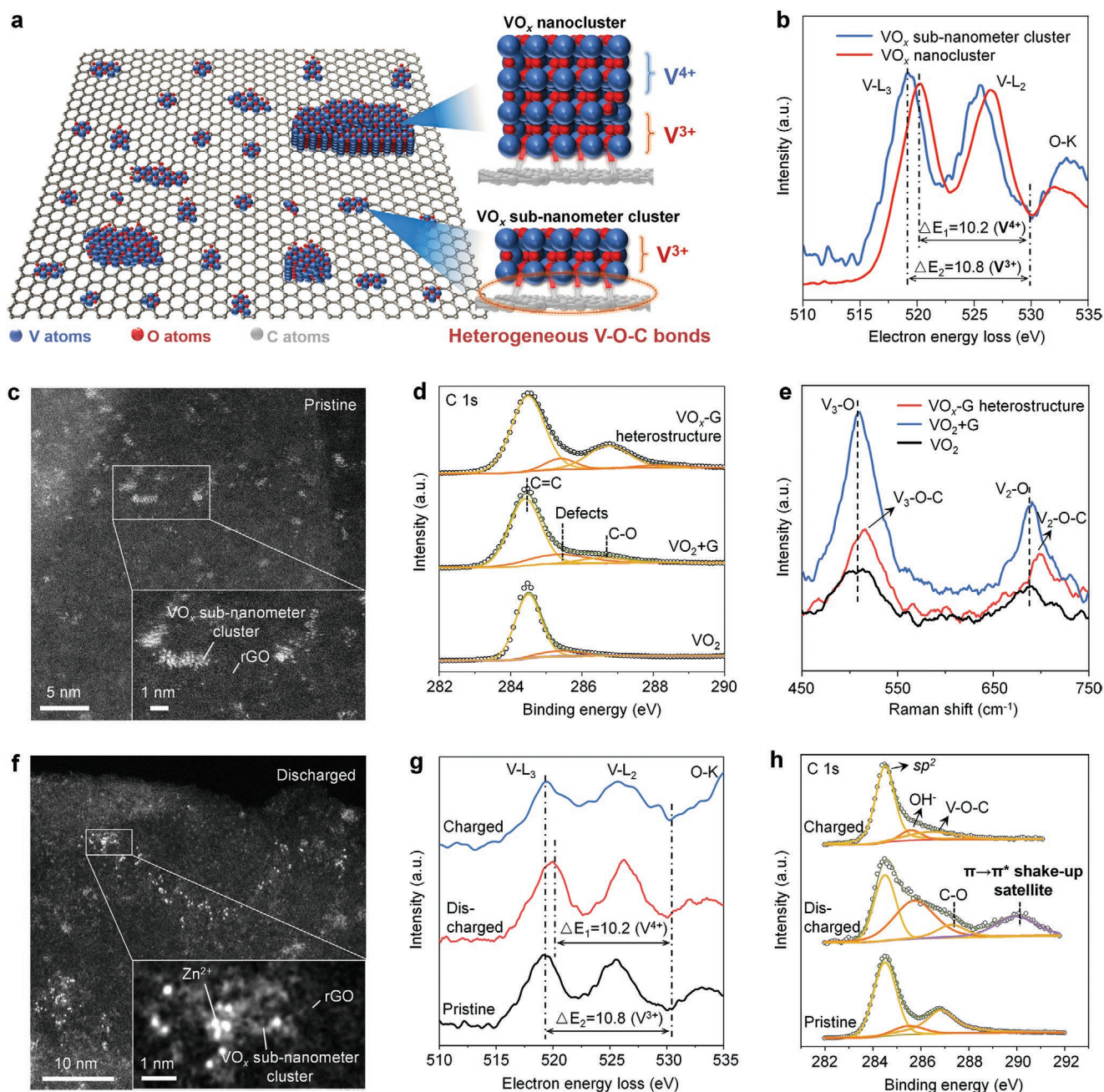
Figure 1. Characterization of the interfacial configuration in the VO$_x$ – G heterostructure and its anomalous Zn^{2+} storage mechanism. a) Schematic diagram of the VO$_x$ – G heterostructure. b) EELS data collected from the VO$_x$ sub-nanometer cluster and VO$_x$ nanocluster regions, in which VO$_x$ sub-nanometer clusters exhibit slightly rougher signal due to smaller size. c) Atomic-resolution HAADF-STEM image of the VO$_x$ – G heterostructure in the pristine state. Insets on the bottom are the enlarged image, and the bright dots are V atoms, as determined by analyzing the contrast. d,e) Comparative Raman spectra (d) and XPS spectra (e) of the VO$_x$ – G heterostructure, VO$_2$ + G and VO$_2$. f) Atomic-resolution HAADF-STEM image of the VO$_x$ – G heterostructure in the discharged state. The higher the atomic number, the brighter the atom is. Combined with the contrast analysis in (b) and (c), the brightest dot is Zn, and the second brightest dot is V. g,h) EELS spectra (g) and XPS spectra (h) of the VO$_x$ – G heterostructure in pristine, discharged, and charged states.

Information). Remarkably, the valence change of V during charging/discharging is opposite to that of previous reports basing on storage in the bulk or on surface of the material,[10] and this unusual phenomenon explains that the Zn^{2+} storage is not dependent of VO$_x$ bulk according to law of conservation of electric charge. On the other hand, ex situ XPS spectra

(Figure 1h) reveal that a new peak attributed to $\pi \rightarrow \pi^*$ shake-up satellites occurs upon discharging pristine VO$_x$ – G heterostructure, which suggests that the PI electrons of rGO increase significantly[25] (i.e., rGO undergoes electrochemical reduction during Zn^{2+} uptake). These exciting results indicate that the conjugated structure of rGO is the origin of the redox reaction
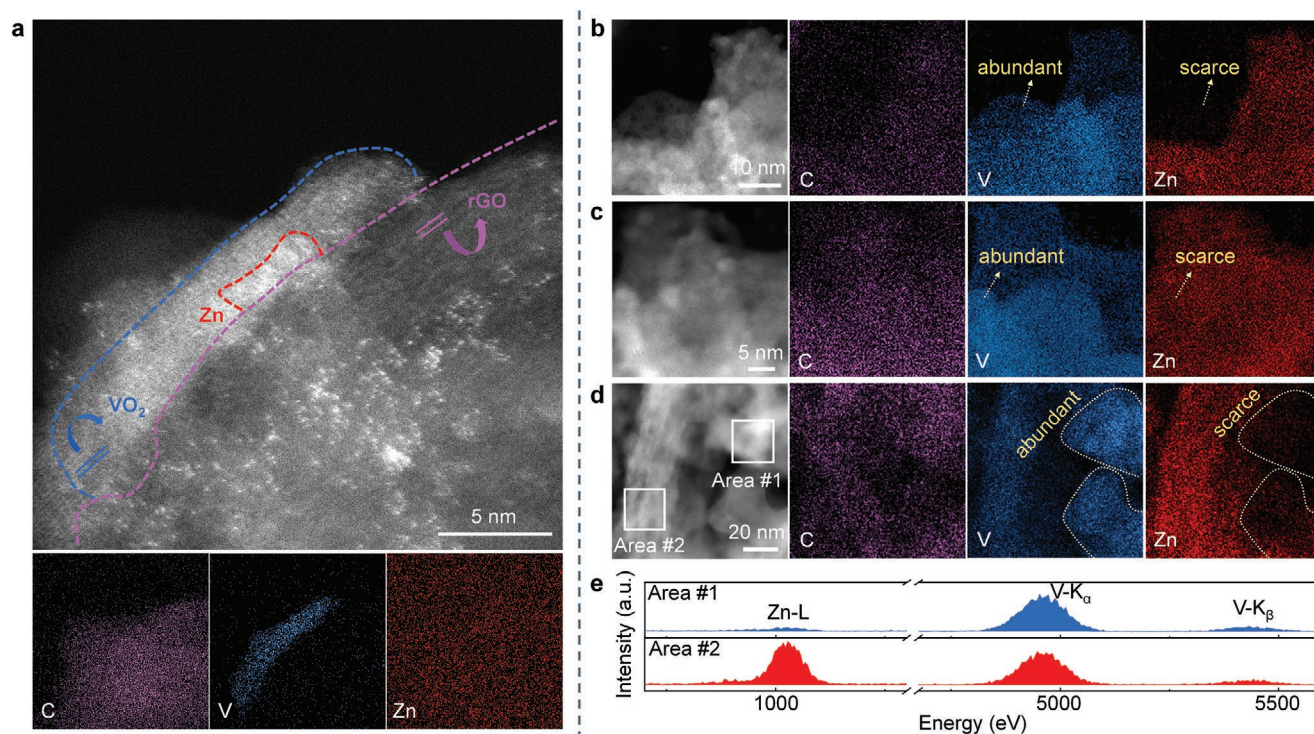
**ADVANCED
SCIENCE NEWS**

www.advancedsciencenews.com

**ADVANCED
MATERIALS**

www.advmat.de

Figure 2. a–d) HAADF-STEM images and corresponding EDS mappings of VO_x – G heterostructure in the fully discharged state. e) EDX spectra recorded from (d).

in Zn^{2+} storage rather than V, which gives rise to a high capacity of 443 mAh g^{-1} at 0.1 A g^{-1} (Figure S12, Supporting Information). Note that pristine rGO shows a low capacity of 6.2 mAh g^{-1} originating from surface ion adsorption.[12] Therefore, the heterogeneous structure endows rGO with the ability to gain and lose electrons (faradaic redox reaction). Combined with Figure 1f, the Zn^{2+} storage relies on both VO_x and rGO, which may be related to the interfacial V−O−C bonds.

More visualized information was provided by HAADF-STEM images and corresponding energy dispersive spectrometer (EDS) mappings obtained in the discharged state (**Figure 2**). As seen from the sectional HAADF-STEM image in Figure 2a, the Zn^{2+} ions predominantly distributed at the interface in VO_x nanocluster regions, which indicates a interfacial Zn^{2+} storage process. At lower-magnification images, we can observe that there are abundant V signals in the areas marked by yellow dotted lines while the Zn signals are extremely scarce (Figure 2b–d). For a clearer display, we selected Figure 2d as an example and performed energy-dispersive X-ray (EDX) in the Area #1 and Area #2, respectively. From the semiquantitative data in the corresponding EDX spectra, we could observe that the Zn content is not dependent on the V content (Figure 2e). The above results suggest that Zn^{2+} ions are stored mainly in the interface between VO_x and rGO, while very few are stored in the VO_x bulk.

To further investigate the structural evolution of VO_x – G heterostructure during Zn^{2+} uptake/extraction, we performed ex situ and in situ XRD analysis. However, the output signal of VO_x is inconspicuous (Figure S13, Supporting Information) owing to the sub-nanometer size. Hence, we carried out ex situ and in situ Raman investigations. As shown in the ex situ Raman spectra (**Figure 3**a), the interfacial V2−O−C bonds

were converted into V−O−V bonds after discharge, suggesting the cleavage of interfacial V−O−C bonds. This phenomenon may be related to Zn^{2+} inserting into the interface between VO_x and rGO, which is consistent with the Zn^{2+} distribution in the HAADF-STEM image (Figure 1f). In a further in situ Raman investigation (Figure 3b; and Figure S14, Supporting Information), interfacial Zn^{2+} storage and reversible break/reconstruction of the interfacial V−O−C bonds were observed more directly. The peaks located at 1067 and 1088 cm^{-1} are attributed to C−O and Zn−O (mode of 2A$_1$(LO), see ref. [26]), respectively. During discharge, the content of C−O gradually decreases, while that of Zn−O gradually increases, suggesting that Zn^{2+} ions are inserted into the interfacial space between VO_x and rGO and are stored through the electrostatic interaction between Zn^{2+} and O by forming V−O−Zn bonds (see Note S3, Supporting Information). Afterward, the inserted Zn^{2+} ions lead to cleavage of heterogeneous V−O−C bonds at deeper discharging states, while more V−O−Zn bonds form. Conversely, the content of V−O−C bonds increases and that of V−O−Zn decreases during Zn^{2+} ion extraction (Figure 3c). The dynamic break/reconstruction of the V−O−C bonds during charging/discharging is termed "interface breathing."

Moreover, the cleavage of heterogeneous bonds during discharging alters the electronic structure of rGO. Figure 3d shows that the inserted Zn^{2+} results in a peak shift of the G-band of rGO, suggesting that the electron–phonon coupling of graphene is altered[24] (which corresponds to the increase in the number of PI electrons of rGO, as shown in Figure 1h). In addition, the defect degree of rGO is reduced (I_D/I_G value decreases from 1.33 to 0.98) due to Zn^{2+} insertion, which is visualized in the corresponding DFT simulations: the interfacially inserted
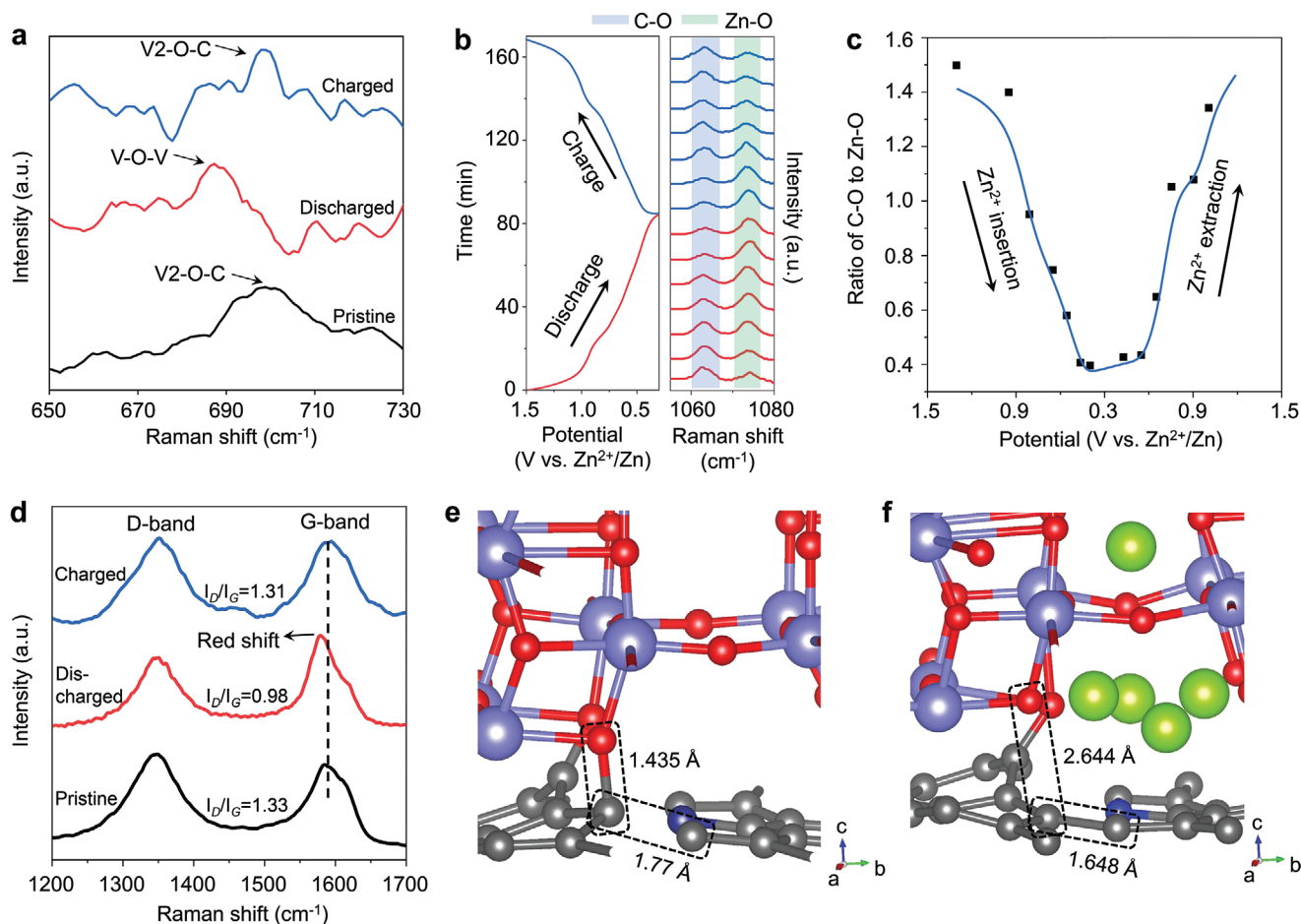
Figure 3. Characterization of interfacial Zn^{2+} storage in the VO$_x$ – G heterostructure. a) Raman spectra between 650 and 730 cm^{-1} in pristine, fully discharged and fully charged states. b) In situ Raman investigation during the 2nd charging/discharging cycle. On the right are the in situ Raman spectra, and on the left are the corresponding galvanostatic charge–discharge curves. c) Quantitative ratio of C—O to Zn—O during discharging/charging, which is collected from (b). d) Raman spectra between 1200 and 1700 cm^{-1} in pristine, fully discharged and fully charged states. e,f) DFT simulations of the VO$_x$ – G heterostructure in pristine (e) and fully discharged (f) states.

Zn^{2+} repels the pristine-bonded C atom to the in-plane of rGO. Combined with the electrons transferred to rGO during discharging (Figure 1h), the reduction in defect degree is additional proof of interfacial Zn^{2+} storage. As a result, we can safely draw the conclusion that Zn^{2+} ions are stored predominantly within the interface between VO$_x$ and rGO, while few in VO$_x$ bulk. To provide a better understanding of the interfacial storage behavior and the above anomalous phenomena, further DFT simulations are employed.

As seen from the simulation of Zn^{2+} diffusion in the bulk and interface, both of the interfacial diffusion and bulk diffusion of Zn^{2+} indicate that the most likely pathway is along the [001] direction (**Figure 4**a,b). The transition states of migration barriers in bulk and interfacial paths are 0.82 and 0.61 eV (Figure 4c,d), respectively. The much lower energy barrier indicates a more feasible Zn^{2+} diffusion path in the interface.

According to ex situ EELS, ex situ XPS, and in situ Raman results, Zn^{2+} diffusion occurs within the interface, and Zn^{2+} storage relies on constraints between interfacial Zn^{2+} and O in VO$_x$ (see Note S3, Supporting Information). In addition, electron conduction occurs on rGO and relies on the conjugated

structure of rGO, which is much faster than in monoclinic VO$_2$ (the latter is semiconducting at room temperature[27]). As a result, theoretically both electronic and ionic transport mechanisms are faster in interface-dominated charge storage than in bulk charge storage. More importantly, based on this decoupled transport of electrons/Zn^{2+} ions in the VO$_x$ – G heterostructure, not only the mobility of electrons and ions is improved, but also an additional enhancement in zinc transport is achieved due to the different electric potentials of the components within the heterostructure: Specifically, we denote the interfacial channel as phase α and rGO as β. Note that interface-dominated storage makes the motion of electron and ion more like a monolayer than traditional transport conditions[14] and hence is highly in line with 1D diffusion process within the space charge region.[17] Zinc diffusion allows (see derivation in Note S4, Supporting Information) the following Equation

$$j_{Zn} = -\frac{1}{F^2}\frac{\sigma_{ion}^{\alpha}\sigma_{eon}^{\beta}}{\sigma_{ion}^{\alpha}+\sigma_{eon}^{\beta}}\left[\frac{\partial\mu_{ion}^{\alpha}}{\partial C_{ion}^{\alpha}}+\frac{\partial\mu_{eon}^{\beta}}{\partial C_{eon}^{\beta}}+F\frac{\partial(\varphi^{\alpha}-\varphi^{\beta})}{\partial C_M}\right]\nabla C_M \quad (1)$$

$$= -D^{\delta}\nabla C_M$$

ADVANCED
SCIENCE NEWS

www.advancedsciencenews.com
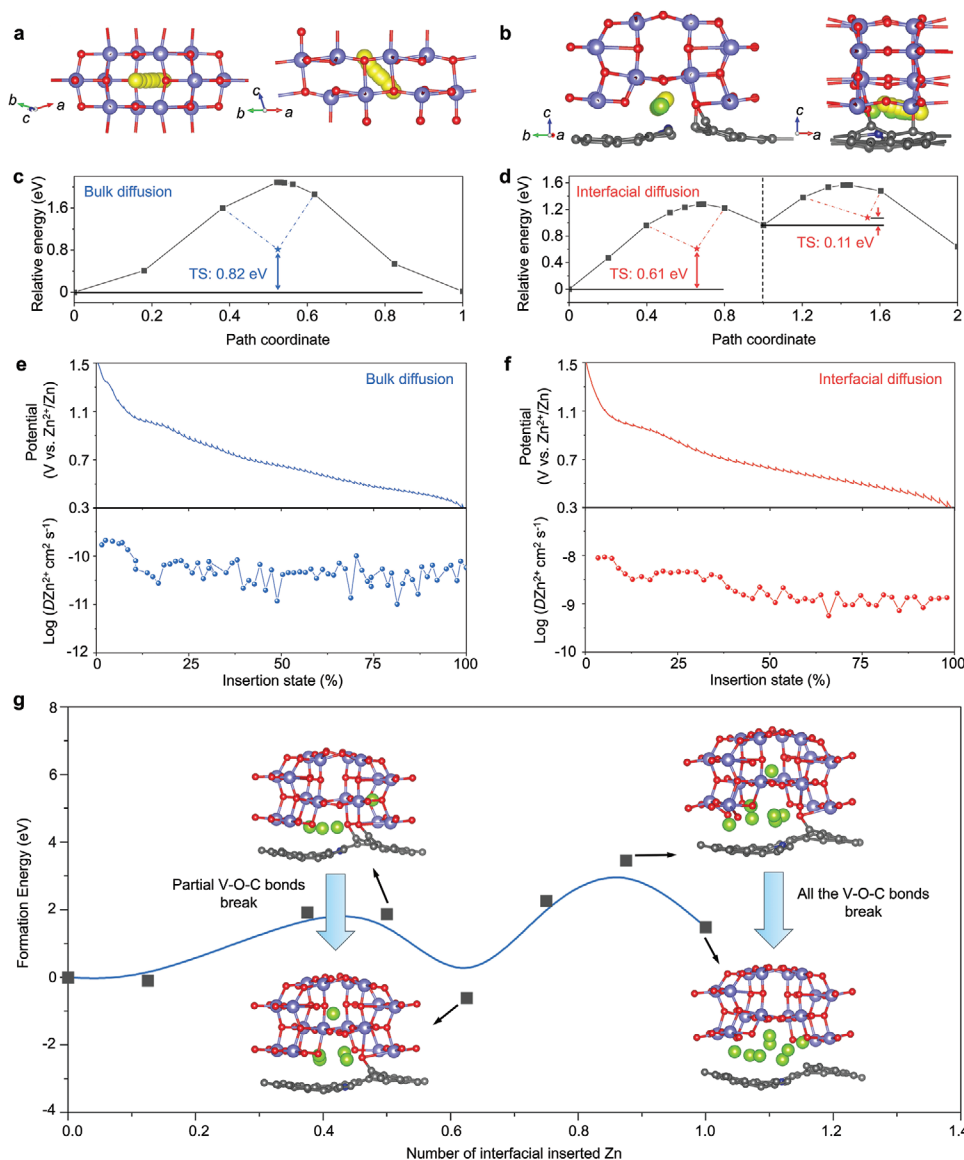
ADVANCED
MATERIALS

www.advmat.de

Figure 4. Theoretical simulations of Zn^{2+} storage in the interface and in the bulk. a,b) Illustration of the Zn diffusion path in the bulk (a) and in the interface (b). c,d) Migration barrier of the Zn^{2+} ion in the VO$_2$ bulk (c) and in the VO$_x$/rGO interface (d). e,f) Discharge GITT curves and corresponding Zn^{2+} coefficients versus discharge depth in VO$_2$ + G (e) and VO$_x$ – G heterostructure (f). g) Formation energy evolution during Zn^{2+} ion insertion into the interface. The inset presents the structure after relaxation under 4-, 5-, 7-, and 8-Zn^{2+} ion insertion conditions.

As the driving force of the diffusive flux is the gradient of the concentration, Equation (1) follows Fick's law and can be abbreviated as the second line in Equation (1). Since both σ_{ion}^{α} and σ_{eon}^{β} are enhanced according to the above analysis, a higher

$\dfrac{\sigma_{ion}^{\alpha}\sigma_{eon}^{\beta}}{\sigma_{ion}^{\alpha}+\sigma_{eon}^{\beta}}$ value is obtained in interface-dominated storage than in the bulk storage. In the meantime, the additional term

$F\dfrac{\partial(\varphi^{\alpha}-\varphi^{\beta})}{\partial C_{M}}$ is zero in bulk diffusion due to the homogeneity, while it is nonzero in interfacial storage arising from the electric field built into the VO$_x$/rGO interface, thus giving rise to the further enhancement of the Zn^{2+} diffusion coefficient (D_{Zn}) during interfacial storage.

Beyond the theoretical analysis, the diffusion coefficient of zinc in the VO$_x$ – G heterostructure at the discharge plateau was experimentally determined to be 5.05×10^{-9} cm^2 s^{-1} through galvanostatic intermittent titration technique (GITT) measurements (Figure 4f). This value is over two orders of magnitude higher than that of VO$_2$ + G (Figure 4e) and previously reported VO$_2$-based cathodes for AZIBs (Table S2, Supporting Information).

On the other hand, the heterogeneous interface is more favorable for cation adsorption. The charge population of the interface is determined through a charge-density-difference diagram (Figure S15a, Supporting Information). As electrons are concentrated at the interfacial V−O−C bond, the interface has the potential to attract positively charged Zn^{2+} from the

ADVANCED
SCIENCE NEWS
www.advancedsciencenews.com

ADVANCED
MATERIALS
www.advmat.de

electrolyte due to opposite polarities. Moreover, we carried out zeta potential analysis and demonstrated that a much more negative charge was obtained due to the formation of interfacial V−O−C bonds in the VO_x − G heterostructure (Figure S15b,c, Supporting Information). Therefore, in addition to faster diffusion kinetics, the adsorption of Zn^{2+} ions is also more accessible in interface-dominated storage than in bulk storage, which contributes to the further improvement of the overall electrochemical reaction kinetics.

We further investigated the theoretical capacity of interface-dominated storage through the intercalation of Zn^{2+} ions into the heterogeneous interface. The corresponding formation energy is recorded in Figure 4g and is calculated according to the following

$$E_b = E_{substrate + nZn} - E_{nZn} - E_{substrate} \qquad (2)$$

It is observed in the inset of Figure 4g; and Videos S1–S6 (Supporting Information) that some of the interfacial V−O−C bonds are broken after five Zn^{2+} ions are inserted, and all the V−O−C bonds are broken after eight Zn^{2+} ions are inserted. As the interfacial V−O−C bonds undergo reversible break/reconstruction during charging/discharging (as shown in Figure 3a–c), interfacial storage would be irreversible only when all interfacial chemical bonds are broken. Therefore, in this simulation, seven Zn^{2+} ions are the limitation of interface-dominated storage (vs interfacial V_8O_{16}), which corresponds to the theoretical capacity of 717.06 mAh g^{-1}. This value is much higher than that of VO_2(B) under the conventional intercalation-reaction machanism (409.75 mAh g^{-1}, as seen in Figure S16, Supporting Information). It is well known that ion storage in the bulk or on the surface of a material relies on the overall integrity of the structure, within which the "lattice breathing" effect harms the structural stability of the electrode material and leads to fast capacity fading.[28] Distinctively, the "interface breathing" effect occurring in the interface stores extra Zn^{2+} ions after partial destruction of the interface, and the interface can be reconstructed after Zn^{2+} ions are extracted, thus enlarging the charge depth and storing more Zn^{2+} ions than in the bulk or surface. Moreover, the tiny spacing change of the VO_2 (110) plane in this simulation is consistent with the ex situ synchrotron high-energy XRD (HEXRD) analysis of the VO_x − G heterostructure (Figure S17, Supporting Information), which demonstrates the reliability of this theoretical simulation.

The electrochemical kinetics of Zn^{2+} storage in the VO_x − G heterostructure are further studied by multisweep rate cyclic voltammetry (CV). The CV curves obtained with sweep rates varying from 0.1 to 2 mV s^{-1} are shown in **Figure 5**a. According to the relationship between the measured current (i) and the sweep rate (v)[29]

$$i = av^b \qquad (3)$$

where a and b refer to adjustable parameters. Specifically, $b = 0.5$ indicates that the current is controlled by semi-infinite linear diffusion, while a value of 1 indicates that the current is surface controlled. The b-value of redox peaks can be determined by plotting $\log i_p$ versus $\log v$ (Figure 5b). When sweep

rates are in the range of <50 mV s^{-1}, the b-values of the four peaks are close to 1 and presented as 0.92, 0.93, 0.97, and 0.98, indicating that the reaction is surface-controlled. Moreover, the correlation between capacity and sweep rate is applied to investigate the rate-limiting step in the charge-storage mechanism (Figure 5c). Analogous to Figure 5b, two separated regions can be clearly observed. In region 1 (sweep rates < 50 mV s^{-1}), the exhibited capacity is mostly independent of sweep rate, indicating that the reaction is surface-controlled, namely, solid-state Zn^{2+} diffusion is not the limiting factor of the rate performance.[30] From Figure 5d,e, the electrochemical dominating step transforms from surface-controlled to diffusion-controlled at 50 mV s^{-1}. This phenomena can be attributed to an increase in the ohmic contribution or zinc diffusion constraints. Note that previous reports[10,31] show an abrupt change from surface-controlled to diffusion-controlled normally arises when the sweep rate increases to 10–20 mV s^{-1}, while the critical value in the VO_x − G heterostructure is about 50 mV s^{-1}. As the surface reaction rate increases when the sweep rate increases, the higher critical value in the VO_x − G heterostructure than conventional storage in the bulk or surface indicates that solid-state Zn^{2+} diffusion in interface-dominated storage is faster and can match faster surface reactions. In a further fitting, the percentage of the capacitive contribution to the whole current at a fixed voltage was evaluated by separating the current i into diffusion-controlled and capacitive contributions.[29] The capacitive contribution of the current in the VO_x − G heterostructure at 0.1 mV s^{-1} is 90.5% and increases to 97.5% at 2 mV s^{-1} (Figure 5d,e). The ultrahigh capacitive contribution at low sweep rates suggests a unique pseudocapacitive effect that has rarely been reported, which can be attributed to the unique interface-dominated reaction sites. This kind of capacitive-dominated behavior contributes to the fast electrochemical kinetics in the VO_x − G heterostructure. We further evaluate the b-value at every 0.05 V and reveal that most of the b-value in the potential window are larger than 0.9 (Figure 5f), indicating a dominated surface-controlled reaction from 0.1 to 2 mV s^{-1}.

Finally, the reaction kinetics of the faradaic charge transfer reaction are evaluated using Nicholson's parameter (Ψ). This parameter can be determined by correlating the change in peak-to-peak potential separation (ΔE_p) and the electron transfer number (n) with varying CV sweep rates. The standard rate constant of the heterogeneous reaction (k^0) of the quasireversible electrochemical reaction can be further determined through plotting Ψ versus $v^{-1/2}$ (to guarantee a quasireversible system, $0.001 < \Psi < 7$ is required) using Equation (4), where the symbols have their usual meaning[32]

$$\Psi = k^0 \left(\frac{RT}{\pi nFD} \right)^{1/2} v^{-1/2} \qquad (4)$$

The slope of Ψ versus $v^{-1/2}$ was determined to be 0.1438 according to the red line in Figure 5g. Therefore, the k^0 of the VO_x − G heterostructure was determined to be 1.18×10^{-4} cm s^{-1}, which is two orders of magnitude higher than that of VO_2 + G (5.84×10^{-6} cm s^{-1}, as shown in Figure S19, Supporting Information). The results indicate that interface-dominated storage can reach equilibrium more rapidly with a much faster redox
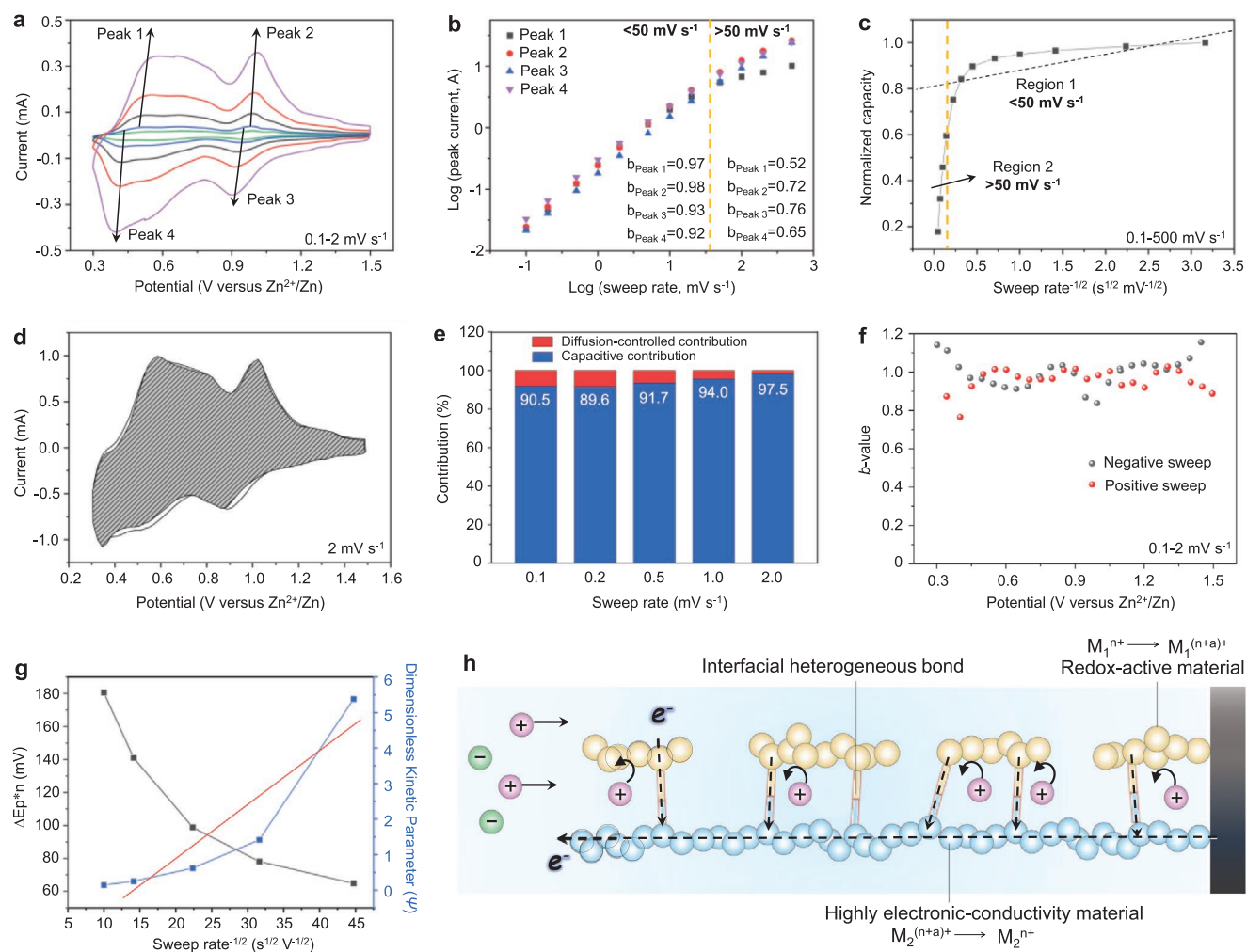
**ADVANCED
SCIENCE NEWS**

www.advancedsciencenews.com

**ADVANCED
MATERIALS**

www.advmat.de

Figure 5. Kinetic analysis of the electrochemical behavior of interfacial Zn^{2+} storage in the $VO_x - G$ heterostructure. a) Cyclic voltammograms from 0.1 to 2 mV s^{-1}. b) Determination of the b-value of redox peaks by evaluating the relationship between the peak current and sweep rate from 0.1 to 500 mV s^{-1} (the original cyclic voltammograms are shown in Figure S18, Supporting Information). c) Capacity versus $v^{-1/2}$ from 0.1 to 500 mV s^{-1} is considered for separating diffusion-controlled capacity from capacitive-controlled capacity. d) Cyclic voltammogram at 2 mV s^{-1}. The capacitive contribution to the total current is expressed as the shaded region. e) Capacitive and diffusion-controlled contributions to capacity from 0.1 to 2 mV s^{-1}. f) Evaluation of the b-value at every 0.05 V in the potential window from 0.1 to 2 mV s^{-1}. g) Nicholson's working curve. The red line is the linear fitting of Ψ versus sweep rate$^{-1/2}$. h) Schematic of the interface pseudocapacitance.

reaction than conventional storage mechanisms in $VO_2 + G$ (see Figures S20 and S21, Supporting Information). The interfacial storage features are summarized in Figure 5h. Faster electron/ion transport can be obtained by being decoupled from the bulk/surface of the pseudocapacitive material, while a higher faradaic reaction rate can then be realized, which is termed interface pseudocapacitance.

For electrochemical performance tests, CR2016 coin-type cells were assembled using $VO_x - G$ heterostructure, $VO_2 + G$, and VO_2 film cathodes. Zinc foil was used as the anode, and a 3 M $Zn(OTf)_2$ aqueous solution was used as the electrolyte to investigate the electrochemical performance. Remarkably, the high reversible capacity of 443 mAh g^{-1} at 100 mA g^{-1} of the $VO_x - G$ heterostructure is much higher than that of $VO_2 + G$ and VO_2 due to their different storage mechanisms (Figure S22, Supporting Information). The high capacity of the $VO_x - G$ heterostructure is reproducible, as

seen in the box plot (Figure S23 and Table S3, Supporting Information).

Moreover, a superior rate performance was observed in the $VO_x - G$ heterostructure, which delivers a capacity of 174.4 mAh g^{-1} at an ultrahigh current density of 100 A g^{-1}, indicating that the battery takes only 6.3 s to be fully discharged (**Figure 6**a,b). Additionally, this rate capability signifies a capacity retention of 39.4% for a 1000-fold increase in current density, which (the capacity retention) to our knowledge is one of the best rate capabilities among AZIBs. In addition, the capacity of the film electrode consisting of rGO and carbon nanotubes (CNTs) is negligible at each current (Figure S24, Supporting Information); therefore, the capacity contributions from carbon materials in the $VO_x - G$ heterostructure are excluded. For comparison with conventional energy storage mechanisms, the previously reported AZIB cathode materials with the highest rate capabilities are summarized in Figure 6c,

ADVANCED
SCIENCE NEWS

www.advancedsciencenews.com

ADVANCED
MATERIALS

www.advmat.de

including Mn_3O_4 (ref. [33], mass loading of ≈2 mg cm^{-2}), V_2CT_x (ref. [34], mass loading of ≈0.8 mg cm^{-2}), and poly(1,5-NAPD)/AC (ref. [35], mass loading of ≈2.7 mg cm^{-2}). Remarkably, with increasing current density, the capacity retention of interface-dominated storage is distinctively higher than that of conventional storage (effective mass loading of the VO$_x$ – G heterostructure is 1.59 mg cm^{-2} as seen in the Experimental Section). Therefore, high-energy and high-power Zn^{2+} storage is achieved when storage predominantly originates from the interface (Figure S25, Supporting Information). Owing to the high-rate ion transport of the interfacial Zn^{2+} storage, it is possible for the VO$_x$ – G heterostructure to work at higher mass loading levels. As shown in Figure 6d, we further assembled VO$_x$ – G heterostructure film electrodes with effective mass loading of 3.18, 6.36, and 12.72 mg cm^{-2}, respectively. At a practical mass loading of 12.72 mg cm^{-2}, the VO$_x$ – G heterostructure still shows 3.67 mAh cm^{-2} at 1.27 mA cm^{-2} and 1.23 mAh cm^{-2} at 127.4 mA cm^{-2}, which corresponds to a more gradual decay in areal capacity compared to other high rate and high mass loading electrodes[35–37] (Figure 6e). Therefore, the interfacial storage is applicable and promising for developing practical high-rate electrodes.

The cycling performance of the VO$_x$ – G heterostructure for interfacial storage is also much better than that of VO$_2$ + G and VO$_2$ (Figure S26, Supporting Information). We

also observed that the profile of the charging/discharging curve of the VO$_x$ – G heterostructure remains almost unchanged after 50 cycles (Figure S27, Supporting Information), indicating a robust structure of the VO$_x$ – G heterostructure that can function well under such deep-charging conditions. Moreover, the VO$_x$ – G heterostructure shows a slower natural voltage recovery than VO$_2$ + G in the discharged state without an applied current or voltage (Figure S28, Supporting Information), demonstrating that the interface anchors Zn^{2+} ions more tightly than bulk/surface sites; hence, interfacial storage is beneficial for practical use conditions when batteries remain unused.

We further adjusted the ratio of VO$_x$ to rGO and discovered that the interfacial zinc storage behavior can be further optimized by constructing electrode materials containing more interface. For instance, we could subtract the thickness of the two components in the interface-containing composite electrode or increase the proportion of interfacial bonding between the two components within the heterogeneous electrode (Figures S29–S31, Supporting Information).

Furthermore, we evaluated the universality of the interfacial Zn^{2+} storage mechanism. Interface-rich composites of rGO@TiO$_2$ and rGO@SnO$_2$ were synthesized and assembled into film electrodes with CNTs. The hybrid cathodes show capacities of about 20–30 mAh g^{-1} at 100 mA g^{-1}. Interestingly, neither

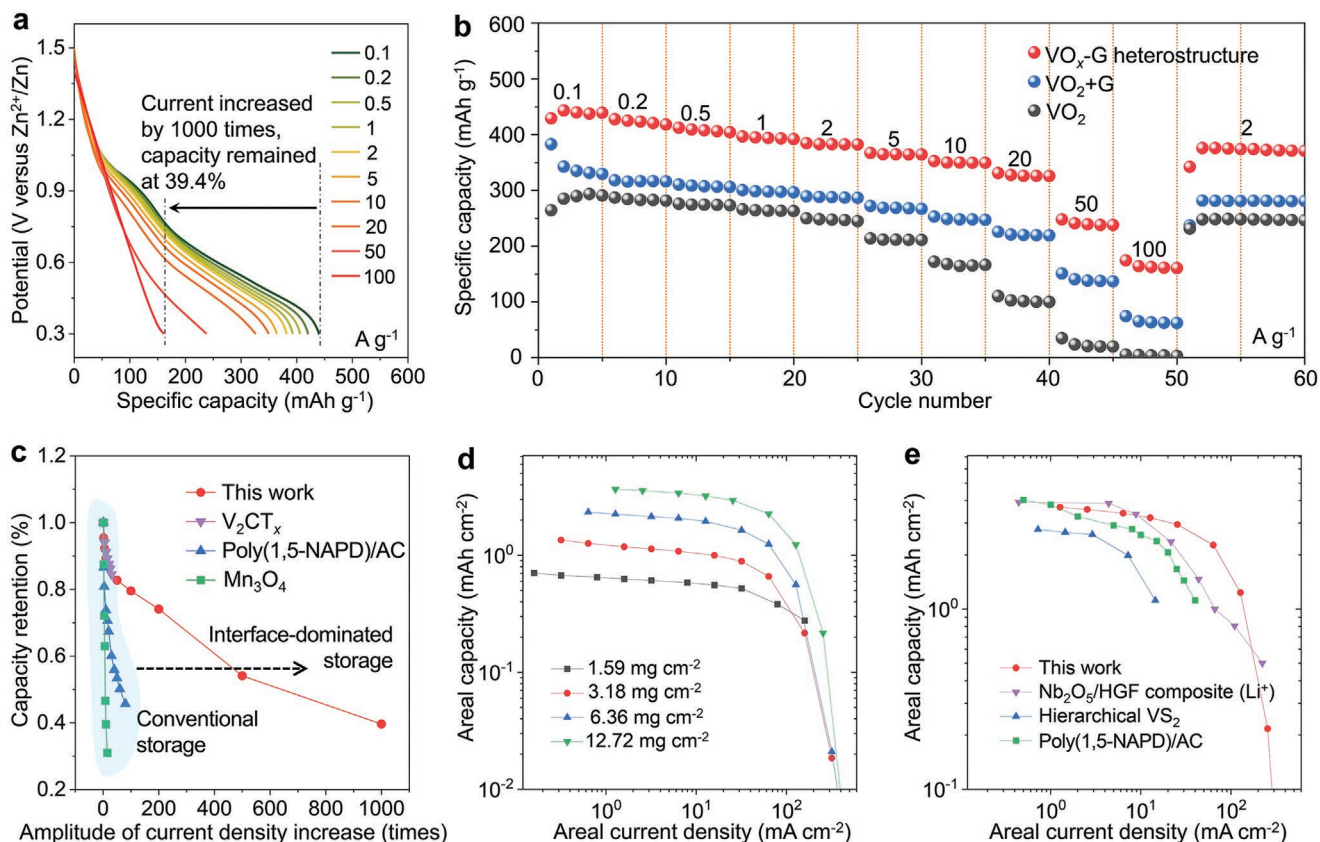**Figure 6.** Electrochemical Zn^{2+} storage performance. a) Galvanostatic discharge curves of the VO$_x$ – G heterostructure varying from 0.1 to 100 A g^{-1}. b) Cycling performance of the VO$_x$ – G heterostructure, VO$_2$ + G and VO$_2$ varying from 0.1 to 100 A g^{-1}. c) Rate capability analysis (comparing the VO$_x$ – G heterostructure to AZIB cathode materials with the highest rate performance reported previously). d) The effect of areal current density and effective mass loading on the areal capacity of the VO$_x$ – G heterostructure. e) Comparison of high mass loading capability of the VO$_x$ – G heterostructure with other high loading materials.

**ADVANCED
SCIENCE NEWS**

www.advancedsciencenews.com

**ADVANCED
MATERIALS**

www.advmat.de

rGO, TiO$_2$, nor SnO$_2$ shows any capability toward Zn^{2+} storage. Therefore, interfacial storage is able to make inactive cathode materials useful, demonstrating the possibility of the extended applications of the interfacial zinc storage mechanism (detailed characterizations and tests are shown in Figures S32–S34, Supporting Information).

3. Conclusion

We have comprehensively investigated the predominant interfacial Zn^{2+} storage behavior in the VO$_x$ – G heterostructure by performing in/ex situ Raman, ex situ EELS, ex situ XPS, and ex situ HAADF-STEM investigations. The predominantly interfacial Zn^{2+} storage mechanism exhibits anomalous valence changes toward VO$_x$ and rGO comparing to conventional mechanisms, and endows rGO the ability of faradaic-active energy storage. Corresponding DFT simulations provide insight into the faster diffusion kinetics and more storage sites of Zn^{2+} in the interface than in the bulk. As the interfacial zinc storage undergoes a decoupled transport of electrons and Zn^{2+}, the built-in electric field of the VO$_x$/rGO interface further accelerates Zn^{2+} diffusion. Moreover, a unique interfacial pseudocapacitive effect with a high rate has also been obtained. Finally, the interfacial Zn^{2+} storage shows a high capacity of 443 mAh g^{-1} at 100 mA g^{-1} and an ultrahigh rate capability of 174.4 mAh g^{-1} at 100 A g^{-1} for the VO$_x$ – G heterostructure. The interfacial storage behavior is also revealed to be highly controllable and applicable for other systems including TiO$_2$–rGO and SnO$_2$–rGO, which realizes the utilization of materials without energy storage capacities. This interface-dominated Zn^{2+} storage mechanism provides new ideas for electrode material design and will act as an exciting avenue for the further development of devices with high energy density and high power density.

4. Experimental Section

Synthesis of the VO$_x$ – G Heterostructure: rGO was synthesized from a modified Hummers method.[38] Additionally, the V$_2$O$_5$ sols were prepared via a melt-quenching process as described elsewhere.[39] In a typical process, 5 mL V$_2$O$_5$ sols (18.55 mg mL^{-1}) was added to a beaker with a well-mixed 5 mL rGO aqueous dispersion (3.15 mg mL^{-1}, namely, 15% rGO with regard to the whole mass of V$_2$O$_5$ and rGO) and 5 mL commercially available n-propanol. After 30 min of stirring and subsequent ultrasonic treatment, the resultant mixed solution was sealed in a Teflon autoclave and reacted at 180 °C for 12 h. After cooling to room temperature naturally, the supernatant liquid was poured out, and the obtained hydrogel-shaped sample was dispersed into deionized (DI) water. Afterward, 46.5 mg CNTs (namely, 30 wt%) were added, and the mixed solution was uniformly distributed by an ultrasonic cell disruptor. Then, the suspension was vacuum filtered with polyethersulfone filter paper (pore size 0.45 μm), followed by washing with DI water. Finally, the VO$_x$ – G heterostructure with effective mass loading of 1.59 mg cm^{-2} was obtained, and the films with higher mass loadings of 1.59, 3.18, 6.36, and 12.72 mg cm^{-2} are assembled using analogous methods.

Synthesis of VO$_2$ + G: For the synthesis of VO$_2$ in VO$_2$ + G, a modified process based on a previous report was applied.[40] Typically, 74 mg NH$_4$VO$_3$ was stirred with 190 μL HCOOH and 40 mL of deionized water until the solution became homogeneous. The resultant precursor was transferred into a sealed 50 mL autoclave and heated at 180 °C

for 12 h. After cooling to room temperature naturally, the precipitates were washed with DI water and ethanol three times. After that, the precursor was dispersed into rGO aqueous solution, in which rGO occupied 15 wt% of the sum of the resultant solid and rGO, and then, physically mixed VO$_2$ and rGO were obtained. Finally, by filtration with CNTs using the same fabrication procedure used to prepare the VO$_x$ – G heterostructure, the VO$_2$ + G film was obtained.

Synthesis of VO$_2$: After synthesizing the same VO$_2$ precursor as VO$_2$ + G, the precipitates were filtered directly with CNTs using a method identical to that used to prepare the VO$_x$ – G heterostructure, making the VO$_2$ film.

Material Characterization: The electrode materials are assembled with CNTs into film electrodes in electrochemical tests, so if not specified, the structural characterizations performed in this work are based on the film state, which is closer to the real working state. The morphologies and crystallographic and microstructural characteristics of the samples were measured using FE-SEM (JEOL-7100F), HAADF-STEM, and EELS (Titans Themis), XRD (D8 Advance X-ray diffractometer with a Cu Kα radiation source), and HEXRD (at beamline 11-ID-C of Advanced Photon Source at Argonne National Laboratory; a beam with a size of 0.2 × 0.2 mm^2 and wavelength of 0.1173 Å was applied to obtain 2D diffraction patterns). The chemical states and atomic structure information were investigated by XPS (Thermo-Fisher Scientific- ESCALAB 250Xi), Raman spectroscopy (DXR, Thermo-Fisher Scientific, with 532 nm excitation from an argon-ion laser), and FTIR (Nexus, Thermo Nicolet).

Electrochemical Characterization: The prepared binder-free films were directly used for electrodes. Electrochemical experiments were conducted based on the coin cell (CR2016-type), using a film punched into an 8 mm round disk as the cathode and Zn metal as the anode. A 3 м Zn(OTf)$_2$ aqueous solution served as the electrolyte. Galvanostatic charge/discharge measurements were performed in the voltage range of 0.3–1.5 V by a multichannel battery testing system (LAND CT2001A) for GITT and 0.1 A g^{-1} tests. The charge/discharge at 20 A g^{-1} as well as the rate performance tests were collected by EC-LAB (VMP-3, Bio-Logic SAS), the higher accuracy of which guarantees steady data collection at a large current density (the rate performance was collected after one cycle of activation at 0.1 A g^{-1}). Additionally, CV and electrochemical impedance spectroscopy were conducted with EC-LAB. All the tests were carried out at room temperature.

The specific capacity of the VO$_x$ – G heterostructure is based on the sum of the masses of both VO$_x$ and rGO. The power density P (W kg^{-1}) and energy density E (Wh kg^{-1}) were calculated according to the following equations

$$E = \int_0^t \frac{IV}{m}dt \tag{5}$$

$$P = \frac{1}{t}\int_0^t \frac{IV}{m}dt \tag{6}$$

where I, V, m, and t are the current, voltage, mass of active materials, and discharging time, respectively. Namely, the energy density E is equal to the integrated area in the curve of the potential versus specific capacity, while the value of E divided by the corresponding discharging time represents the power density P.

Simulations: Based on the crystal structure parameters of X-ray diffraction analysis combined with XPS results, Raman spectra, and FTIR spectra of the prepared VO$_x$ – G heterostructure powder and VO$_x$ – G heterostructure film, a visualization model is established with density functional theory calculation to simulate the ion implantation barrier, volume expansion coefficient, and ion optimal diffusion path of vanadium oxide. The thermodynamics and kinetics of the diffusion barrier are also studied. At the same time, the electronic structure, band structure, and charge distribution of the material after ion implantation are analyzed, and the internal mechanism of the influence of the vanadium oxide layer structure on its electrochemical performance is determined.

**ADVANCED
SCIENCE NEWS**

www.advancedsciencenews.com

**ADVANCED
MATERIALS**

www.advmat.de

DFT calculations are based on the CASTEP high-precision electronic structure quantitative calculation module in Materials Studio software. The generalized gradient approximation and Perdew–Burke–Ernzerhof exchange correlation functionals are used to describe the electron density gradient information of atoms in materials. In the meantime, the van der Waals interaction between the vanadium oxide layer structures was described using dispersion correction DFT-D method. The crystal structures of the vanadium pentoxide and VO_x – G heterostructure were established. The geometry optimization parameters were set as follows: plane wave expansion was performed with an energy cut-off of 500 eV, the K-point grid of the Brillouin zone was sampled by the Monkhorst-Pack method, the value was set to $4 \times 4 \times 4$ for pure VO_2 bulk crystal and $3 \times 4 \times 1$ for the VO_x – G heterostructure. The convergence conditions of energy and force were 1×10^{-5} eV and 0.03 eV Å^{-1}, respectively.

Supporting Information

Supporting Information is available from the Wiley Online Library or from the author.

Conflict of Interest

The authors declare no conflict of interest.

Data Availability Statement

Research data are not shared.

[1] M. Armand, J. M. Tarascon, *Nature* **2008**, *451*, 652.

[2] B. Dunn, H. Kamath, J. M. Tarascon, *Science* **2011**, *334*, 928.

[3] D. Kundu, B. D. Adams, V. Duffort, S. H. Vajargah, L. F. Nazar, *Nat. Energy* **2016**, *1*, 16119.

[4] H. Pan, Y. Shao, P. Yan, Y. Cheng, K. S. Han, Z. Nie, C. Wang, J. Yang, X. Li, P. Bhattacharya, K. T. Mueller, J. Liu, *Nat. Energy* **2016**, *1*, 16039.

[5] Q. Zhao, W. Huang, Z. Luo, L. Liu, Y. Lu, Y. Li, L. Li, J. Hu, H. Ma, J. Chen, *Sci. Adv.* **2018**, *4*, eaao1761.

[6] L. Wang, K. W. Huang, J. Chen, J. Zheng, *Sci. Adv.* **2019**, *5*, eaax4279.

[7] D. Bin, W. Huo, Y. Yuan, J. Huang, Y. Liu, Y. Zhang, F. Dong, Y. Wang, Y. Xia, *Chem* **2020**, *6*, 968.

[8] M. Yan, P. He, Y. Chen, S. Wang, Q. Wei, K. Zhao, X. Xu, Q. An, Y. Shuang, Y. Shao, K. T. Mueller, L. Mai, J. Liu, J. Yang, *Adv. Mater.* **2018**, *30*, 1703725.

[9] F. Wan, Y. Zhang, L. Zhang, D. Liu, C. Wang, L. Song, Z. Niu, J. Chen, *Angew. Chem., Int. Ed.* **2019**, *58*, 7062.

[10] J. Ding, Z. Du, L. Gu, B. Li, L. Wang, S. Wang, Y. Gong, S. Yang, *Adv. Mater.* **2018**, *30*, 1800762.

[11] L. Fu, C.-C. Chen, J. Maier, *Solid State Ionics* **2018**, *318*, 54.

[12] P. Simon, Y. Gogotsi, B. Dunn, *Science* **2014**, *343*, 1210.

[13] H. Jiang, D. Ren, H. Wang, Y. Hu, S. Guo, H. Yuan, P. Hu, L. Zhang, C. Li, *Adv. Mater.* **2015**, *27*, 3687.

[14] C. Chen, H. Xu, T. Zhou, Z. Guo, L. Chen, M. Yan, L. Mai, P. Hu, S. Cheng, Y. Huang, J. Xie, *Adv. Energy Mater.* **2016**, *6*, 1600322.

[15] C.-C. Chen, J. Maier, *Nat. Energy* **2018**, *3*, 102.

[16] P. Balaya, H. Li, L. Kienle, J. Maier, *Adv. Funct. Mater.* **2003**, *13*, 621.

[17] C. C. Chen, L. Fu, J. Maier, *Nature* **2016**, *536*, 159.

[18] Y. F. Zhukovskii, P. Balaya, E. A. Kotomin, J. Maier, *Phys. Rev. Lett.* **2006**, *96*, 058302.

[19] W.-M. Liu, Q. Sun, Z.-W. Fu, *Electrochem. Commun.* **2013**, *27*, 156.

[20] C. Chen, Y. Wen, X. Hu, X. Ji, M. Yan, L. Mai, P. Hu, B. Shan, Y. Huang, *Nat. Commun.* **2015**, *6*, 6929.

[21] H. Asayesh-Ardakani, A. Nie, P. M. Marley, Y. Zhu, P. J. Phillips, S. Singh, F. Mashayek, G. Sambandamurthy, K.-b. Low, R. F. Klie, S. Banerjee, G. M. Odegard, R. Shahbazian-Yassar, *Nano Lett.* **2015**, *15*, 7179.

[22] V. Datsyuk, M. Kalyva, K. Papagelis, J. Parthenios, D. Tasis, A. Siokou, I. Kallitsis, C. Galiotis, *Carbon* **2008**, *46*, 833.

[23] S.-H. Lee, H. M. Cheong, M. Je Seong, P. Liu, C. E. Tracy, A. Mascarenhas, J. R. Pitts, S. K. Deb, *J. Appl. Phys.* **2002**, *92*, 1893.

[24] J. Lee, K. S. Novoselov, H. S. Shin, *ACS Nano* **2011**, *5*, 608.

[25] H. Zarrin, D. Higgins, Y. Jun, Z. Chen, M. Fowler, *J. Phys. Chem. C* **2011**, *115*, 20774.

[26] T. C. Damen, S. P. S. Porto, B. Tell, *Phys. Rev.* **1966**, *142*, 570.

[27] F. J. Morin, *Phys. Rev. Lett.* **1959**, *3*, 34.

[28] L. Huang, Q. Wei, X. Xu, C. Shi, X. Liu, L. Zhou, L. Mai, *Phys. Chem. Chem. Phys.* **2017**, *19*, 13696.

[29] T. Brezesinski, J. Wang, S. H. Tolbert, B. Dunn, *Nat. Mater.* **2010**, *9*, 146.

[30] V. Augustyn, J. Come, M. A. Lowe, J. W. Kim, P. L. Taberna, S. H. Tolbert, H. D. Abruna, P. Simon, B. Dunn, *Nat. Mater.* **2013**, *12*, 518.

[31] N. Liu, X. Wu, L. Fan, S. Gong, Z. Guo, A. Chen, C. Zhao, Y. Mao, N. Zhang, K. Sun, *Adv. Mater.* **2020**, *32*, 1908420.

[32] R. S. Nicholson, *Anal. Chem.* **1965**, *37*, 1351.

[33] L. Jiang, Z. Wu, Y. Wang, W. Tian, Z. Yi, C. Cai, Y. Jiang, L. Hu, *ACS Nano* **2019**, *13*, 10376.

[34] Y. Liu, Y. Jiang, Z. Hu, J. Peng, W. Lai, D. Wu, S. Zuo, J. Zhang, B. Chen, Z. Dai, Y. Yang, Y. Huang, W. Zhang, W. Zhao, W. Zhang, L. Wang, S. Chou, *Adv. Funct. Mater.* **2020**, *31*, 2008033.

[35] Y. Zhao, Y. Wang, Z. Zhao, J. Zhao, T. Xin, N. Wang, J. Liu, *Energy Storage Mater.* **2020**, *28*, 64.

[36] T. Jiao, Q. Yang, S. Wu, Z. Wang, D. Chen, D. Shen, B. Liu, J. Cheng, H. Li, L. Ma, C. Zhi, W. Zhang, *J. Mater. Chem. A* **2019**, *7*, 16330.

[37] H. Sun, H. Mei, J. Liang, Z. Zhao, C. Lee, H. Fei, M. Ding, J. Lau, M. Li, C. Wang, X. Xu, G. Hao, B. Papandrea, I. Shakir, B. Dunn, Y. Huang, X. Duan, *Science* **2017**, *356*, 599.

[38] Z. Li, Q. He, X. Xu, Y. Zhao, X. Liu, C. Zhou, D. Ai, L. Xia, L. Mai, *Adv. Mater.* **2018**, *30*, 1804089.

[39] C. Zhou, L. Mai, Y. Liu, Y. Qi, Y. Dai, W. Chen, *J. Phys. Chem. C* **2007**, *111*, 8202.

[40] T. Wei, Q. Li, G. Yang, C. Wang, *J. Mater. Chem. A* **2018**, *6*, 8006.